Ultrasonics Sonochemistry 95 (2023) 106362

Contents lists available at ScienceDirect

Ultrasonics Sonochemistry

journal homepage: www.elsevier.com/locate/ultson

Simple sonochemical synthesis, characterization of $TmVO_4$ nanostructure in the presence of Schiff-base ligands and investigation of its potential in the removal of toxic dyes

Atefeh Panahi [a], Mojgan Ghanbari [a], Elmuez A. Dawi [b], Rozita Monsef [a], Russul Reidh Abass [c], Aseel M. Aljeboree [d], Masoud Salavati-Niasari [a,*]

[a] Institute of Nano Science and Nano Technology, University of Kashan, P.O. Box 87317-51167, Kashan, Iran
[b] Nonlinear Dynamics Research Center (NDRC), Ajman University, Ajman P.O. Box 346, United Arab Emirates
[c] Al-Farahidi University, Medical Lab. Techniques Department, College of Medical Techology, Iraq
[d] Chemistry Department, College of Sciences for Women, University of Babylon, Iraq

ARTICLE INFO

Keywords:
Sonochemical
Water contamination
Thulium Vanadate Nanostructures
Toxic Dyes, Eriochrome black T

ABSTRACT

Thulium vanadate (TmVO4) nanorods were successfully prepared by a simple sonochemical approach using Schiff-base ligands. Additionally, $TmVO_4$ nanorods were employed as a photocatalyst. The most optimal crystal structure and morphology of TmVO4 have been determined and optimized by varying Schiff-base ligands, the molar ratio of H2Salen, the sonication time and power, and the calcination time. A Eriochrome Black T (EBT) analysis revealed that the specific surface area was 24.91 m2/g. A bandgap of 2.3 eV was determined by diffuse reflectance spectroscopy (DRS) spectroscopy, which makes this compound suitable for visible photocatalytic applications. In order to assess the photocatalytic performance under visible light, two anionic dyes (EBT) and cationic dyes (Methyl Violet (MV)) were used as models. A variety of factors have been studied in order to improve the efficiency of the photocatalytic reaction, including dye type, pH, dye concentration, and catalyst loading. Under visible light, the highest efficiency was achieved (97.7%) when 45 mg TmVO4 nanocatalysts were present in 10 ppm Eriochorome Black T at pH = 10.

1. Introduction

As a result of population growth, increasing urbanization, rapid industrialization, overuse of natural resources, and widespread use of unsustainable resources, the atmosphere suffers irreversible, detrimental, and severe damage. Various industries and human activities produce wastewater and effluents that endanger our natural resources [1,2]. Every day, millions of gallons of sewage are released by industries such as paper, textiles, chemicals, pulp, pesticides, fertilizers, metal plating, food processing, batteries, pharmaceutical industries, and refineries, contaminating the terrestrial ecosystem and water bodies around us. A variety of contaminants can be found in sewage, including organic (pesticides, dyes, fertilizers, surfactants, pharmaceutical ingredients, phenols, organohalides, etc.), inorganic (metal oxides, heavy metal ions, salts, metal complexes, etc.), pathogens, agricultural runoff, and nutrients [3,4]. In recent years, organic pollutants have received extensive attention because of their widespread use and consequent depletion of terrestrial lands and water bodies, their ability to persist for an extended period of time, and their significant effects on the environment and human health [5,6]. Persistent organic pollutants (POPs) are very resistant to decomposition and degradation, and therefore, they may have detrimental effects on the health of humans and other living organisms [7]. It has been hypothesized that POPs may cause cancer, genetic disabilities, immune and reproductive dysfunction, which will adversely affect the growth of children and infants [8]. Among the most significant categories of organic contaminants are pesticides, dyes, phenolic substances, pharmaceutical ingredients, plasticizers, hydrocarbons, fertilizers, etc. [9,10]. The use of dyes as coloring agents is prevalent in a wide variety of industries, including plastics, textiles, paper, leather, carpets, food, cosmetics, and printing [11]. The textile industry alone consumes about 10,000 tons of dyes each year, of which approximately 10–15% are released as effluents [12]. Consequently, the untreated discharge of effluents from these enterprises into rivers, lakes, and seas is the primary cause of water pollution. As well as being

* Corresponding author.
E-mail address: salavati@kashanu.ac.ir (M. Salavati-Niasari).

https://doi.org/10.1016/j.ultsonch.2023.106362
Received 8 December 2022; Received in revised form 3 March 2023; Accepted 6 March 2023
Available online 9 March 2023

unsightly, highly colored trash blocks light from entering water bodies, thereby disrupting the environmental balance [13].Scheme 1.

In the field of water treatment and environmental decontamination, semiconductor-based photocatalysis is one of the most popular green methods. This manufacturing technique relies on exposing an appropriate semiconductor - usually some transition metal oxides or sulfides - to UV or visible photons of sufficient intensity to form electron and hole pairs (e^-/h^+) in the semiconductor's conduction and valence bands, respectively. The potent and non-selective superoxide and hydroxyl radicals can be produced by the photogenerated electrons and holes reacting with the dissolved oxygen and water molecules (or OH anions), respectively. The organic contaminants present in media can be attacked by these radicals and the photogenerated e^-/h^+ pairs, which can then fragment them into smaller pieces and mineralize them into water and carbon dioxide [14–16].

Among the most significant azo dyes, Eriochrome Black T (EBT), is used to dye silk, wool, nylon, and multifiber materials and as a complexometric titrant for the determination of Ca^{2+}, Mg^{2+}, and Zn^{2+} in laboratories. Even the intermediate component of the extremely harmful dye EBT, naphthoquinone, has a higher level of carcinogenicity. There has been only a limited amount of research conducted in the literature on the effective decolorization of this dye due to an important concern for the effective treatment of wastewater, including EBT and other organic pollutants [17]. Methyl Violet (MV) or pentamethylpararosaniline chloride ($C_{24}H_{28}N_3Cl$) is one of the most common triphenylmethane dyes. In addition to being highly soluble in water, this cationic dye is also highly resistant to photolysis caused by sunlight, oxidizing agents, and aerobic attacks. It is commercially available as a mixture containing tetramethyl- and hexamethylpararosanilines and is primarily used as a source of intense violet color in copying papers and printing inks, as well as a source of deep colors suitable for dyeing cotton, silk, paper, bamboo, weed, straw, and leather [18]. The use of MV is also common in chemical laboratories as a pH indicator, in microbiological laboratories as an antiallergenic and bactericidal agent, and in analysis of Gram's stain for primary bacterial classification and Flemming triple stain with iodine [19].

One of the most significant compounds is vanadate, which is used in a variety of applications, including implantable cardiac defibrillators (ICDs) [20], optical devices [21], catalysts [22,23], and cathodes in batteries [24,25]. A vanadium atom can exist in four adjacent oxidation states as a result of its chemistry. A variety of methods have been employed to prepare thulium vanadate ($TmVO_4$), a type of rare earth (RE) orthovanadate [26,27]. $TmVO_4$ powders are well-known for their electrical, photocatalytic, catalytic, photoluminescence, laser, and optic properties [28–30]. The study of $TmVO_4$ preparation is crucial because $TmVO_4$ is a novel photocatalyst with high catalytic activity in the visible light region [31]. In this regard, we have reported the production of $TmVO_4$ nanoparticles by sonochemical means using Schiff-base ligands

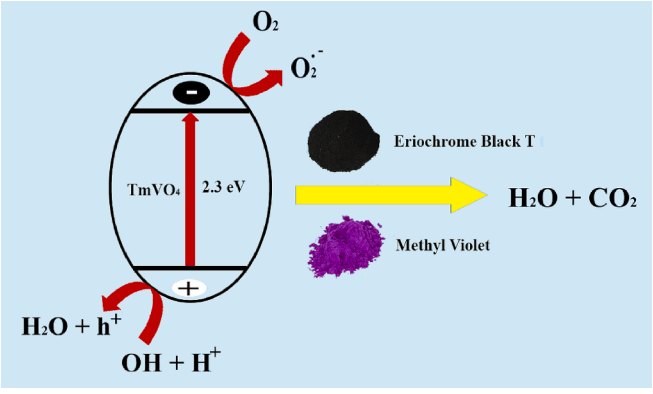

Scheme 1. Schematic diagram of the mechanism for the photodegradation of $TmVO_4$ nanostructures over EBT and MV.

H_2Salen and H_2Salophen as capping and precipitating agents for the control of particle size and shape. Having successfully fabricated $TmVO_4$ nanoparticles and evaluated their optical properties, the photocatalytic behavior of $TmVO_4$ was examined by degrading toxic dyes under visible light. A variety of parameters including pH, dye types, dye concentrations, and catalyst dosage were studied for their effect on photocatalytic performance.

2. Materials and methods

2.1. Materials

Ammonium metavanadate (NH_4VO_3), Thulium Nitrate Hexahydrate ($Tm(NO_3)_3{\cdot}6H_2O$), N, N'-Bis(salicylidene)ethylenediamine (H_2Salen), N, N′-bis(salicylidene)-1,2-phenylenediamine (H_2Salophen), and methanol, were acquired from Merck company and applied without further purification. In addition, the organic dyes utilized as pollutants, such as eriochrome black T (EBT), methyl violet (MV), benzoic acid (BA), benzoquinone (BQ), and Ethylenediaminetetraacetic acid (EDTA) were acquired from Sigma-Aldrich.

2.2. Fabrication of $TmVO_4$

250 mg (0.7 mmol) $Tm(NO_3)_3$, 82 mg (0.7 mmol) NH_4VO_3, were separately dissolved in 10 mL of distilled water. 188 mg H_2Salen (0.7 mmol) (or 190 mg H_2Salophen) was dissolved in 20 mL of methanol. H_2Salen (or H_2Salophen) solution was added to $Tm(NO_3)_3$ solution under stirring. The homogenized solution was placed in an ultrasound device (MPI Ultrasonics; welding, 1000 W, 20 KHz, Switzerland) under ultrasound waves with a power of 60 W for 3 min. The solution containing NH_4VO_3 was added drop-wise to the solution under ultrasonic waves for 30 min until the reaction was complete. After the addition of the solution containing NH_4VO_3, the color of the solution changed from pale yellow to dark green. After completion of the reaction, the precipitate was centrifuged and washed several times with distilled water and then dried in an oven at 70° C for 12 h. Finally, the powder was calcined at 550 ℃ for 6 h. Different conditions were changed to obtain the desired sample (Table 1).

2.3. Photocatalytic process

The catalytic behavior of the $TmVO_4$ nano photocatalyst was assessed by employing two different dyes as toxic contaminants under visible rays. 50 mg of $TmVO_4$ and 15 ppm of dye solution (methyl violet and eriochrome black T) were mixed and moved to a quartz beaker. The suspension was irradiated by visible light (Osram light, Irradiation power; 150 W, Light intensity: 4,000 lm, Volts: 120 V, Luminous flux: 2,400 lm, Wavelength: 400–700 nm) after reaching the adsorption equilibrium of toxic contaminant molecules on the $TmVO_4$ surface. The light source and quartz vessel were housed in an opaque box with a fan to bypass radiation leakage. Influential factors, including dye types, catalyst content, dye concentration, and pH dye adjustment, were assessed for improving the photodegradation ability of $TmVO_4$. The absorbance of samples was measured using a UV–Vis spectrometer at specific time intervals. The dye's degradation percentage (D.P.) was calculated using equation (1). The initial and t-time concentrations of the dye solution should be monitored in this equation.

$$D.P. = \frac{(C_0 - C_t)}{C_0} \times 100 \quad (1)$$

3. Results and discussion

3.1. Crystal structure

XRD patterns for $TmVO_4$ prepared with H_2Salen and H2Salophene as

Table 1
Different conditions for preparation of $TmVO_4$.

Sample No.	Types of Ligands	Molar ratio Tm:V:Ligand	Method	Sonication Time (min)	Sonication Power (W)	Calcination Time (h)
1	H_2Salen	1:1:1	Ultrasound	30	60	6
2	H_2Salophen	1:1:1	Ultrasound	30	60	6
3	H_2Salen	1:1:0.5	Ultrasound	30	60	6
4	H_2Salen	1:1:2	Ultrasound	30	60	6
5	H_2Salen	1:1:2	Ultrasound	15	60	6
6	H_2Salen	1:1:2	Ultrasound	45	60	6
7	H_2Salen	1:1:2	Ultrasound	30	80	6
8	H_2Salen	1:1:2	Ultrasound	30	40	6
9	H_2Salen	1:1:2	Ultrasound	30	60	7
10	H_2Salen	1:1:2	Ultrasound	30	60	8
11	H_2Salen	1:1:2	Ultrasound	30	60	9
12	H_2Salen	1:1:2	Ultrasound	30	60	5

ligands are shown in Fig. 1a and 1b. These patterns are consistent with the characteristic peaks of $TmVO_4$ with reference code 082–1975 and a tetragonal structure. With a molar ratio of 1:1, H_2Salen and H_2Salophene can produce pure $TmVO_4$ when calcined at 600 °C. Fig. 1c and 1d illustrate the effect of different molar ratios of H2Salen to V and Tm. As can be seen in the figure, TmVO4 with the JCPDS card number 082–1975 and tetragonal structure forms when the molar ratios are 1:1:0.5 and 1:1:2. Figs. Fig. 2a and 2b demonstrate how sonication power affects the formation of $TmVO_4$. There is a good match between the patterns and the reference code 082–1975. Further, calcination time had no effect on the crystallinity degree of $TmVO_4$ (Fig. 2c and 2d).

3.2. Mechanism of formation

In general, water is pyrolyzed into H• and OH• radicals during ultrasonic processing. The sonochemical method relies on these highly active radicals. According to the mechanism proposed in this work, VO_3^- may diminish in the presence of H_2O_2 to form VO_4^{3-}. During this sequence of reactions, each radical OH• or H• is capable of generating H_2O_2. OH• and H• radicals can interact in a variety of ways, as shown in the following examples:

$$H_2O \xrightarrow{ultrasonic\ irradiayion} H\cdot + OH\cdot \quad (2)$$

$$H\cdot + H\cdot \rightarrow H_2 \quad (3)$$

$$OH\cdot + OH\cdot \rightarrow H_2O_2 \quad (4)$$

$$H\cdot + O_2 \rightarrow HO\cdot_2 \quad (5)$$

$$H\cdot + HO\cdot_2 \rightarrow H_2O_2 \quad (6)$$

$$HO\cdot_2 + HO\cdot_2 \rightarrow H_2O_2 + O_2 \quad (7)$$

In the reaction between OH• and H• radicals, HO•$_2$ radicals can be formed. In addition, two HO•$_2$ radicals may react to produce H_2O_2. It is also possible to generate hydrogen peroxide by reacting two OH• radicals with ten OH• radicals in the opposite reaction equation. In spite of this, both OH radicals and H radicals appear to have an influence on the production process [32]. It is possible for the first precursors to dissolve into ions that produce water. In the proposed study, the initial precursors are ionic and non-volatile. Thus, the majority of the solution and the cavitation bubbles undergo a reaction. Due to their low vapor pressure, ionic precursors are unable to reach the inner zone of cavitation bubbles. By using the following sonication technique, the ions listed above may react under the appropriate circumstances to form nanosized $TmVO_4$. In Equation (5), VO_3 ions can be reduced to $VO4^{3-}$ ions using an H_2O_2 solution during sonication. At the end of this process, Tm^{3+} interacts with $VO4^{3-}$ ions to form $TmVO_4$ nanoparticles [33]. According to the reaction shown below, it appears that hydrogen peroxide and the end product react directly, and the amount of $TmVO_4$ nanostructures and hydrogen peroxide are positively correlated. Consequently, increasing the production of H_2O_2 increases the nucleation rate. Rapid nucleation produces small particles, resulting in a large number of nuclei, and shortening the crystallization process. Ultrasonic techniques can assist in the rapid production of hydrogen peroxide, resulting in a smaller size and shorter time for the development of products [34].

$$NH_4VO_3 + H_2O \rightarrow NH_4 + + VO_3^- + H^+ + OH^- \quad (8)$$

$$VO_3^- + H_2O_2 \xrightarrow{ultrasonic\ irradiayion} VO_4 + H_2O \quad (9)$$

$$Tm(NO_3)_3.6H_2O \rightarrow Tm^{3+} + 3NO_3 + H_2O \quad (10)$$

$$Tm^{3+} + VO_4 \rightarrow TmVO_4 \quad (11)$$

$$NO_3^- + NH_4^+ \rightarrow NH_4NO_3 \quad (12)$$

$$NH_4VO_3 + Tm(NO_3)_3 + H_2O_2 \rightarrow TmVO_4 + NH_4NO_3 + 2NO_3^- + OH^- + H^+ \quad (13)$$

Furthermore, numerous bubbles formed during the sonochemical process, which led to the pulse waves popping and obliterating. The surfaces of particles and nanoparticles created by the release of bubble-defeating energy may be affected by these phenomena. In response to particle collisions, morphology, scale, and structure have all been significantly altered.

3.3. Bond structure

We present in Fig. 3a and 3b the FT-IR spectra of $TmVO_4$ before and after calcination to study the bonding structures and chemical interactions. Fig. In Fig. 3a, $TmVO_4$ is shown before it has been calcined. As can be seen in Fig. 3a, different peaks can be seen in the $TmVO_4$ spectrum that indicate the presence of H_2Salen on the surface of the $TmVO_4$ nanostructures. In this spectrum, it is evident that all characteristic peaks of H_2Salen are present. The stretching vibration of O-H groups of adsorbed water can be attributed to the absorption at 3425 cm^{-1} [35]. The intense peak at 1637 cm^{-1} was caused by C = N, and the peak that was placed at 2925 cm^{-1} belongs to CH_2 in the H_2Salen ligand structure. The absorption bands at 1210 and 1287 cm^{-1} are assigned to C-O stretching modes. V-O band and VO_4 stretching vibration are detected at 847 cm^{-1} and 454 cm^{-1}, respectively [36]. The band at 1384 cm^{-1} belongs to C-H bending vibration [37]. A FTIR spectrum of $TmVO_4$ after calcination can be seen in Fig. 3b, which shows that the peaks associated with the compound H_2Salen have disappeared. In Fig. 3c, the results of EDS analyses of $TmVO_4$ nanostructures are presented in order to identify the elemental composition and chemical purity. Tm, V, and O lines can be seen clearly in Fig. 3c without any

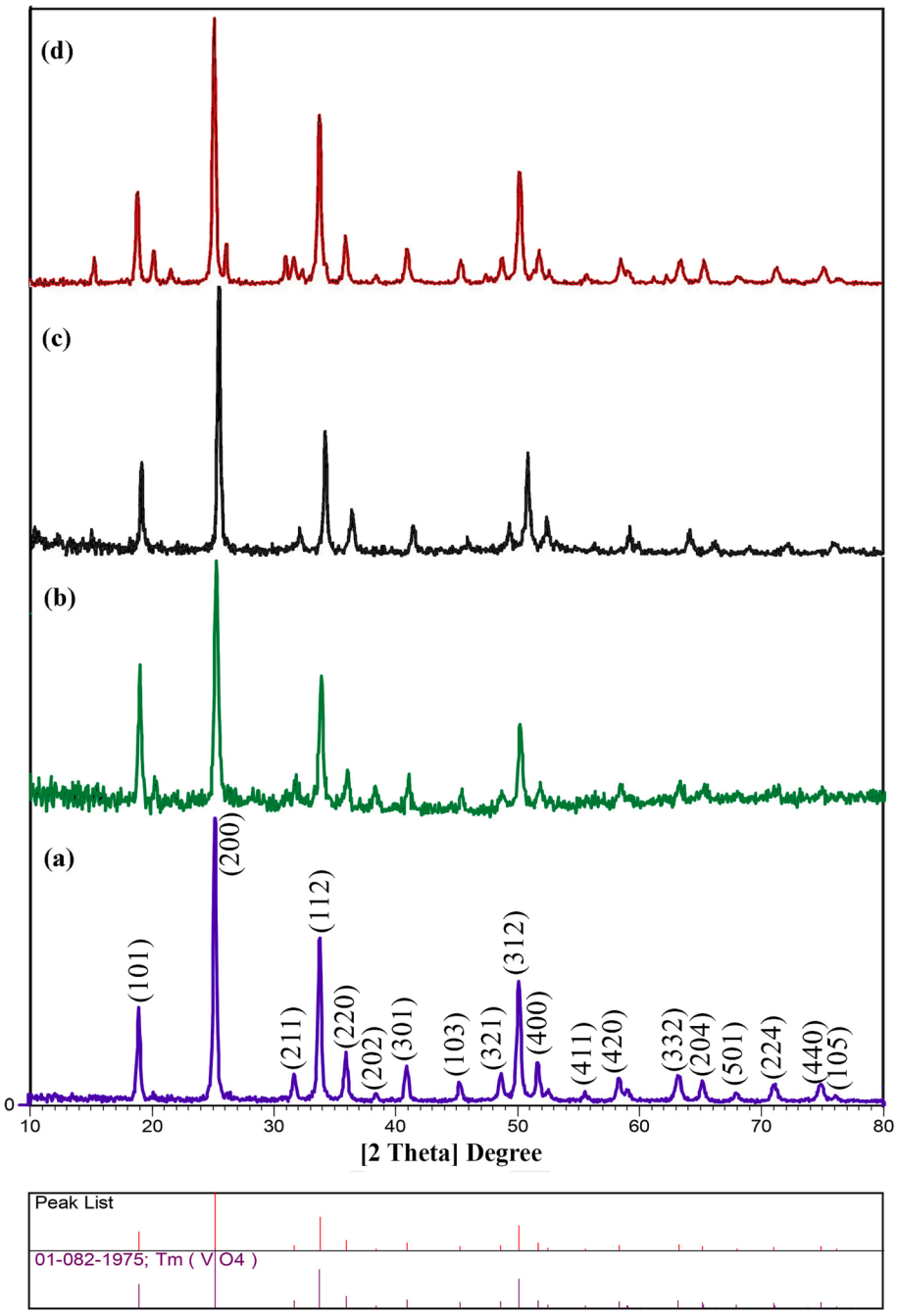

Fig. 1. XRD patterns of $TmVO_4$ preprared in the presence of different ligands a) H_2Salen, b) H_2Salophene, of different molar ratios of Tm:V: ligands c) 1:1:0.5, and d) 1:1:2 with sonication power and time 60 W and 30 min at 550°C for 6 h.

impurities.

3.4. Morphology studies

FESEM microscopy was used to determine the particle diameter as well as the morphology of $TmVO_4$ structures (Fig. 4). After thermal treatment, the morphology, uniformity, size, and shape of the samples are influenced by a number of factors, including ligand type, precursor molar ratio, sonication power and duration, and calcination time.

Fig. 4a and 4b illustrate the surface morphology of $TmVO_4$ in the presence of H_2Salen and H_2Salophene. In these micrographs, it can be observed that Nanoparticles produced in the presence of H_2Salen are more uniform and smaller in size than those produced in the presence of H_2Salophene. Among the most important parameters that can affect the morphology is the molar ratio of the ligand to the metal. Figs. As shown in Fig. 4a, 4c, and 4d, Tm:V:H_2Salen has several molar ratios, such as 1:1:1, 1:1:0.5, and 1:1:2. The figures demonstrate that homogenous nanoparticles are formed in the presence of all three molar ratios. $TmVO_4$ particles in the presence of a 1:1:2 M ratio are smaller than two other particles. Therefore, a 1:1:2 M ratio was selected as the desired ratio. Schiff-base ligands, such as H_2Salen, can be bound to the crystal surfaces of $TmVO_4$ and inhibit crystal growth, resulting in a structure of tiny particles composed of $TmVO_4$. Due to the steric hindrance effect, increasing the concentration of H2Salen ligand by a factor of two results in increased particle sizes, whereas lower concentrations of ligand (1:1 and 1:0.5) result in smaller particle sizes. These phenomena are caused by unfinished ligand coverings on crystal surfaces, which cause particles to enlarge into large structures. Additionally, the time of sonication can

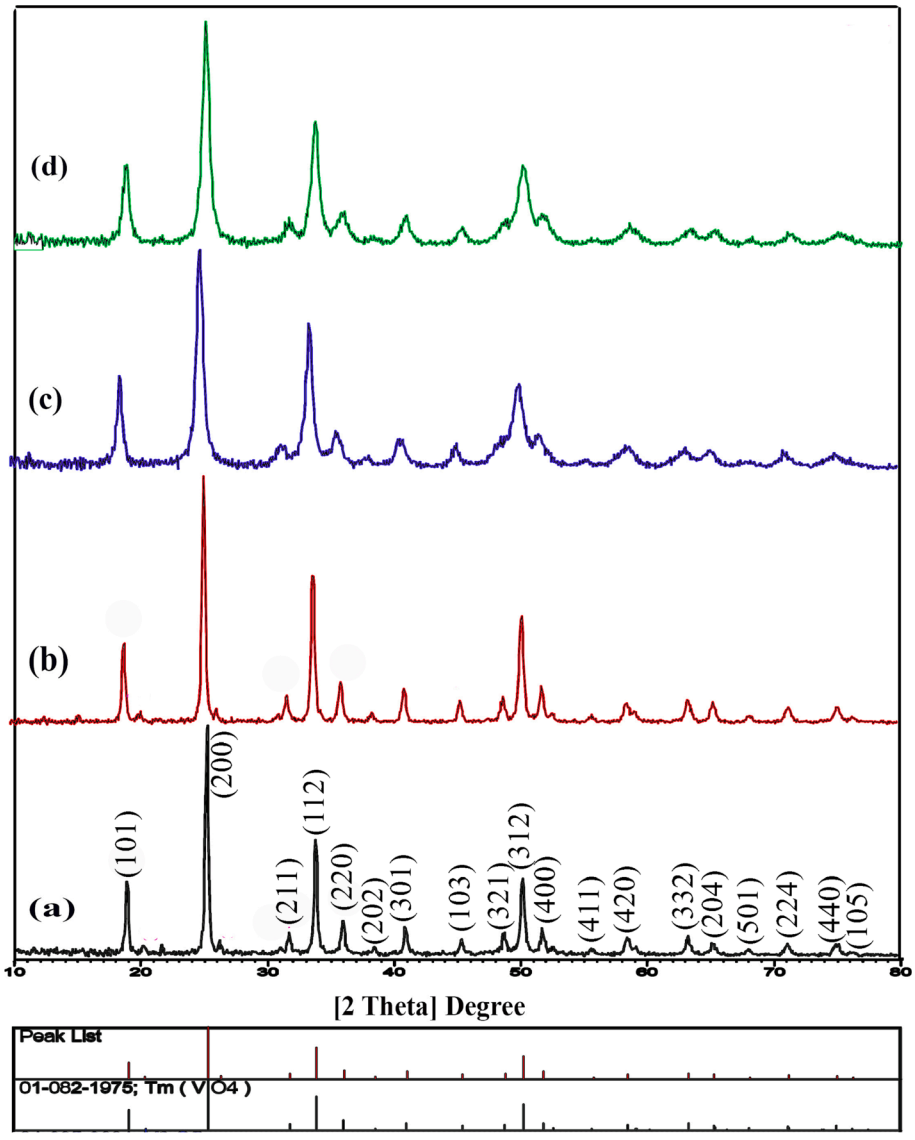

Fig. 2. XRD patterns of $TmVO_4$ preprared with different sonication powers a) 80 W, b) 40 W for 30 min sonication time, different calcination times c) 7 h, and d) 5 h.

have a significant impact on the shape and morphology of products. The figures in 4d, 4e, and 4f illustrate the morphology of $TmVO_4$ prepared after 30 min, 15 min, and 45 min of sonication at constant power. In the presence of ultrasound, a certain threshold of time (30 min) causes the destruction of large particles and the formation of nanoparticles. When the ultrasound time is increased from 30 min to 45 min, the particle size grows due to an increase in the reaction temperature. FESEM images of $TmVO_4$ are shown in Fig. 4d, 5a, and 5b at various sonication powers (60 W, 80 W, and 40 W) and for a constant period of time (30 min). In Fig. 4d and 5a the trend of increasing particle size is clearly visible when the sonication power is increased from 60 W to 80 W. Micro-sized particles are formed due to the increasing reaction temperature that leads to particle agglomeration. In contrast, reducing the ultrasound power can also result in bulk structures. Specifically, increasing the power from 40 W (Fig. 5b) to 60 W (Fig. 4d) results in a reduction in particle diameter and an increase in uniformity. An extreme situation occurs when a cavitation bubble collapses, inducing both chemical and physical reactions. As a result of the implosive collapse of bubbles, which spreads out into the liquid medium, a shock wave is created. The shock wave can accelerate solid particles that are suspended in liquid. A particle's morphology, particle size distribution, and surface composition can be altered by collisions between particles, which may occur at speeds exceeding hundreds of meters per second. It is therefore evident that particles are fragmented. By varying the sonication power, nanostructures can be altered as far as their homogeneity and size are concerned. Consequently, the optimum conditions were obtained at 60 W, 30 min of sonication, and a 1:2 M ratio of metal to ligand at 600 °C for 6 h. Likewise, controlling the morphology and particle size of a product depends on the calcination time. In Fig. 5c, 5d, and 5e, the morphology of $TmVO_4$ at a variety of calcination temperatures (7 h, 8 h, 9 h, and 5 h) can be seen. An increase in calcination time from 6 h to 7 h results in very uniform nanorods (Fig. 5c). As calcination time is increased to 8 h and 9 h, the diameter of the nanorods increases. Consequently, increasing the time to 9 h resulted in the formation of microrods adjacent to the nanoparticles (Fig. 5e). Fig. 5f illustrates how sphere-like nanoparticles are produced by decreasing the calcination time to 5 h. Using comprehensive preparation status control, the most efficient parameters for the fabrication of $TmVO_4$ were determined. In view of its size and uniformity for photocatalytic application, sample No. 9 was determined to be the most efficient sample. It is evident from these figures that when ultrasonic irradiation is used, particle structure is unified. Ultrasonic irradiation causes high pressure and temperature in a solution through the formation of bubbles and the collapse of bubbles. As a result of cavitation surrounding solid particles, the bubble

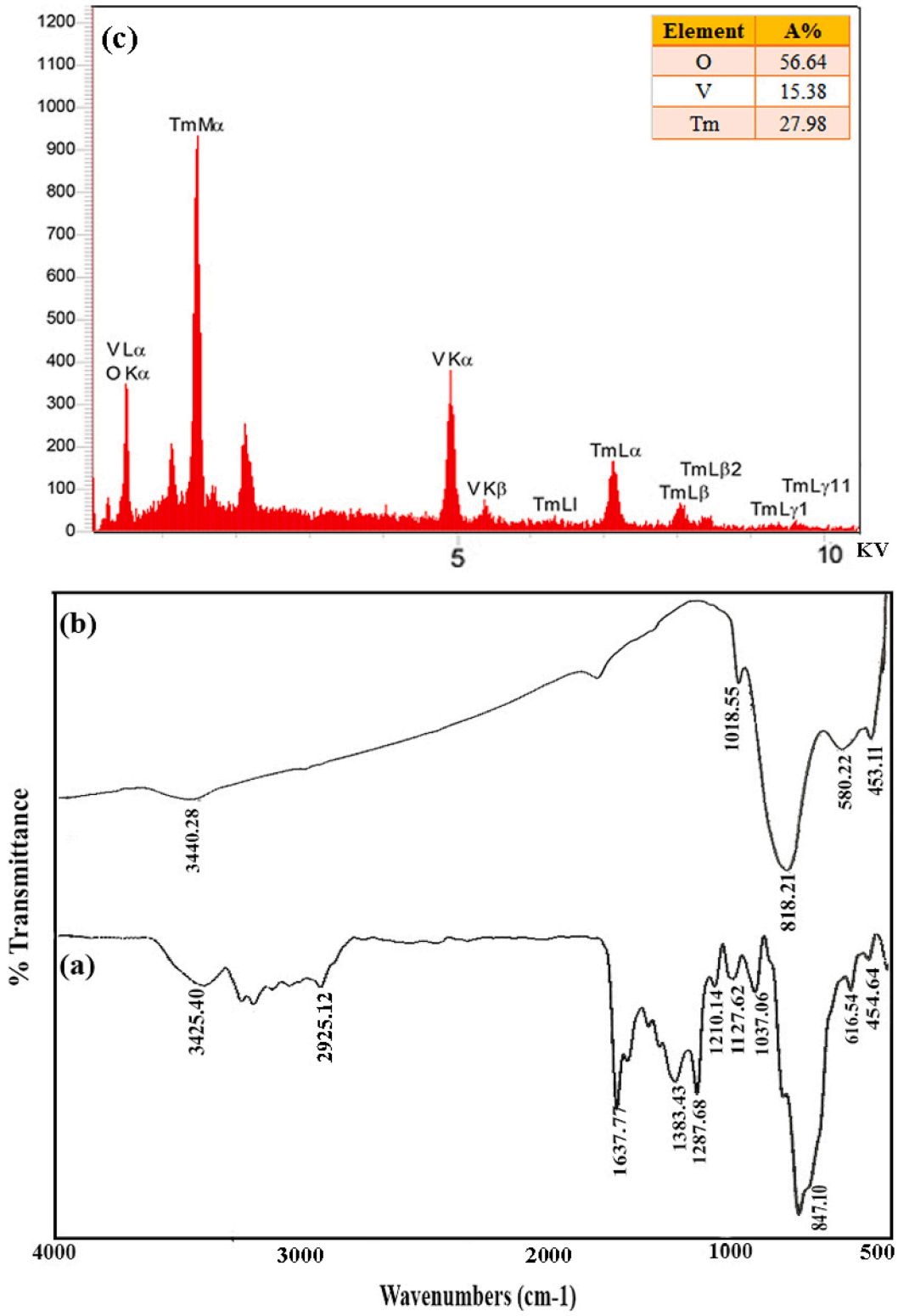

Fig. 3. FTIR spectra a) before, b) after calcination, and c) EDS spectrum of $TmVO_4$ prepared at 30 min, 60 W sonication and 7 h calcination time (Sample 9).

degradation symmetry is altered when the cavitation occurs around the particle. Conversely, the collapse of a bubble that occurs far from the particle causes extremely turbulent flow in the solution as a result of cavitation [38,39]. Thus, the different structures of nanoparticles are created by ultrasonic irradiation under various conditions due to cavitation. TEM micrographs were taken (Fig. 6) to determine the surface morphology of the best sample (sample 9). As can be seen in the photographs taken with the TEM, nanorods are clearly visible.

3.5. BET isotherm

Using the BET method, a standard instrumentation for measuring nitrogen adsorption isotherms at 77 K, the surface area and pore volume of samples can be determined. In Fig. 7a and 7b, the

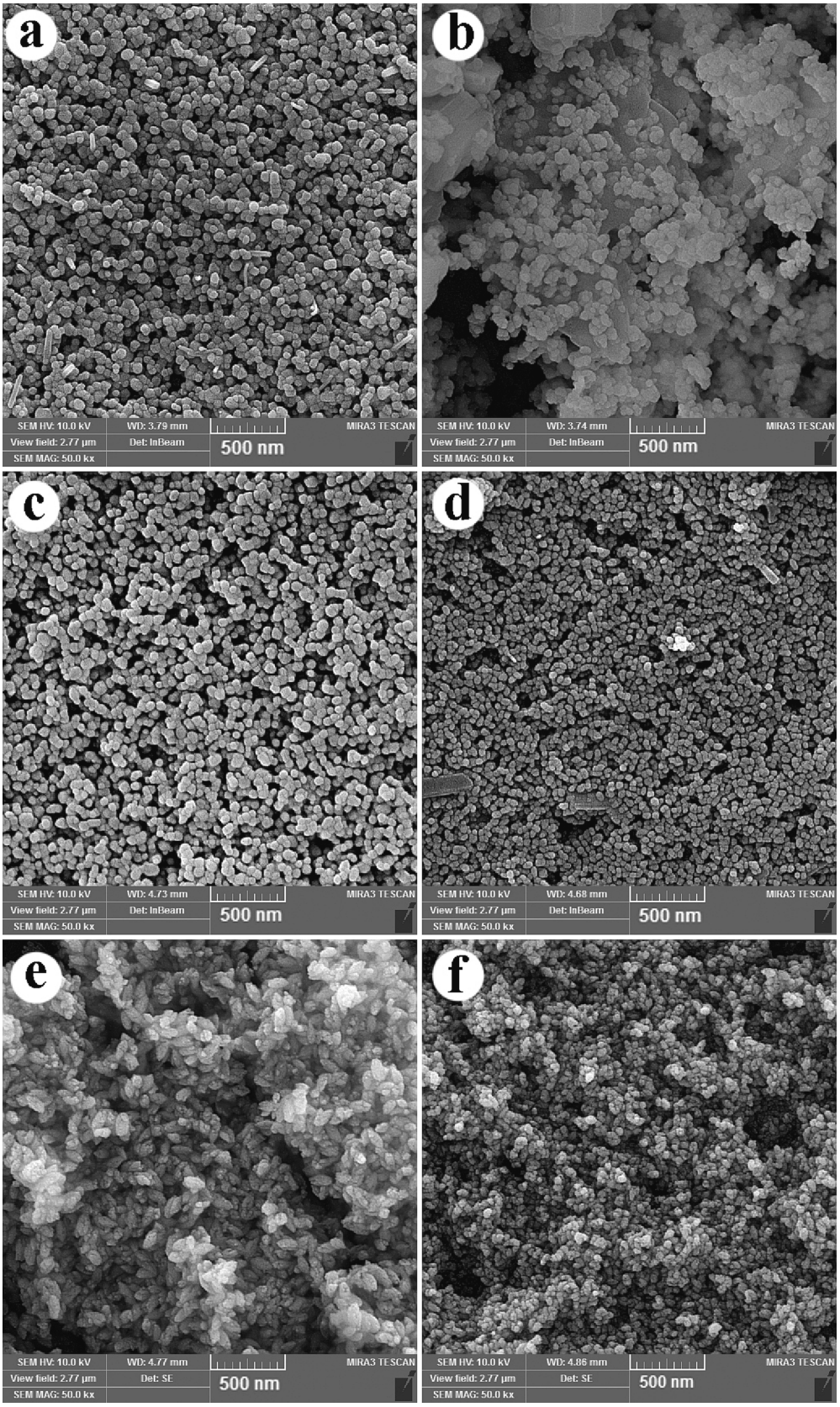

Fig. 4. FESEM micrographs of $TmVO_4$ prepared in different conditions a) H_2Salen, b) H_2Salophene ligands, c)1:1:0.5, d) 1:1:2 Tm:V:H_2Salen molar ratios, e) 15 min, and f) 45 min sonication times.

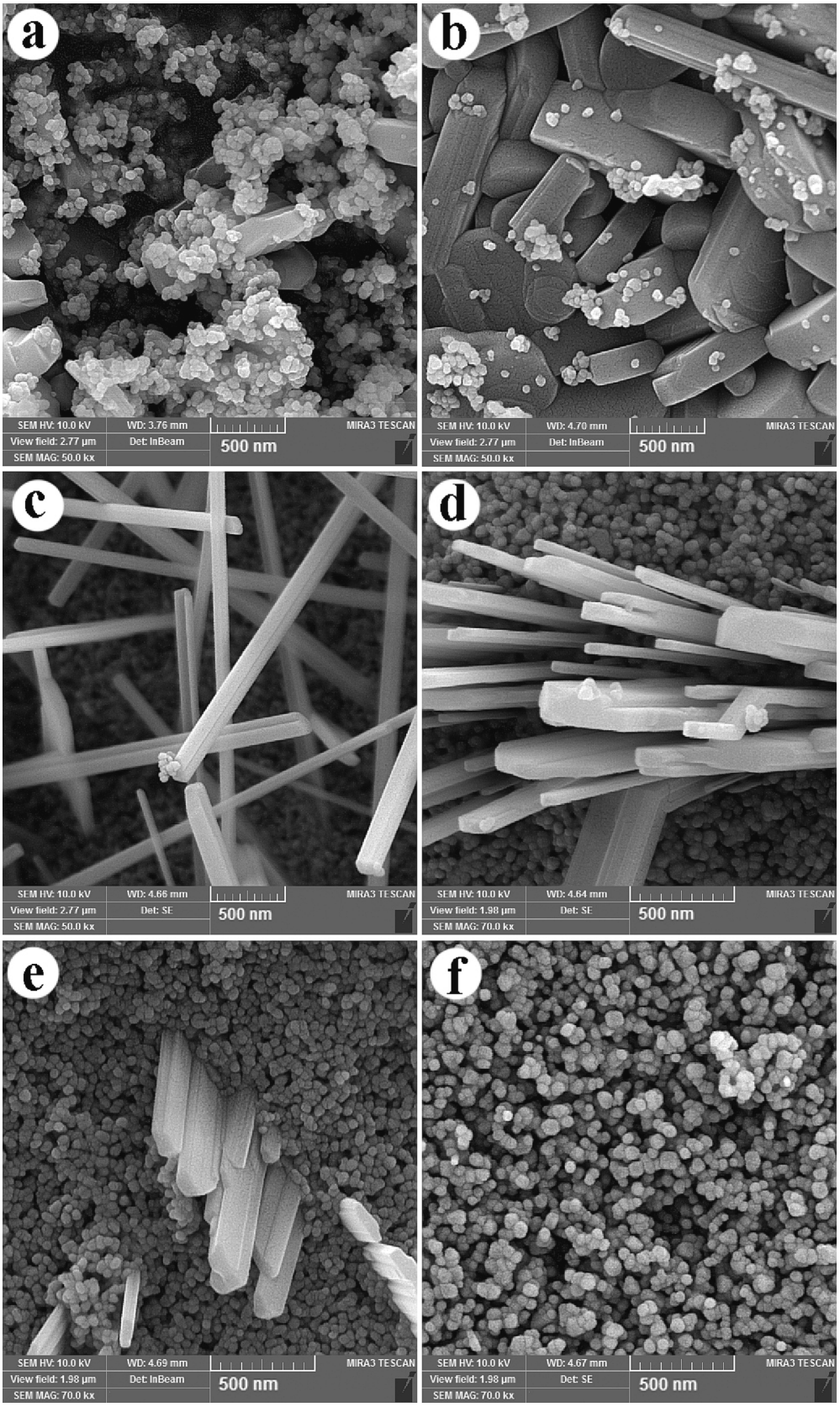

Fig. 5. FESEM micrographs of $TmVO_4$ prepared in different conditions a) 80 W, b) 40 W sonication powers, different calcination times c)7h, d) 8 h, e) 9 h, and f) 5 h.

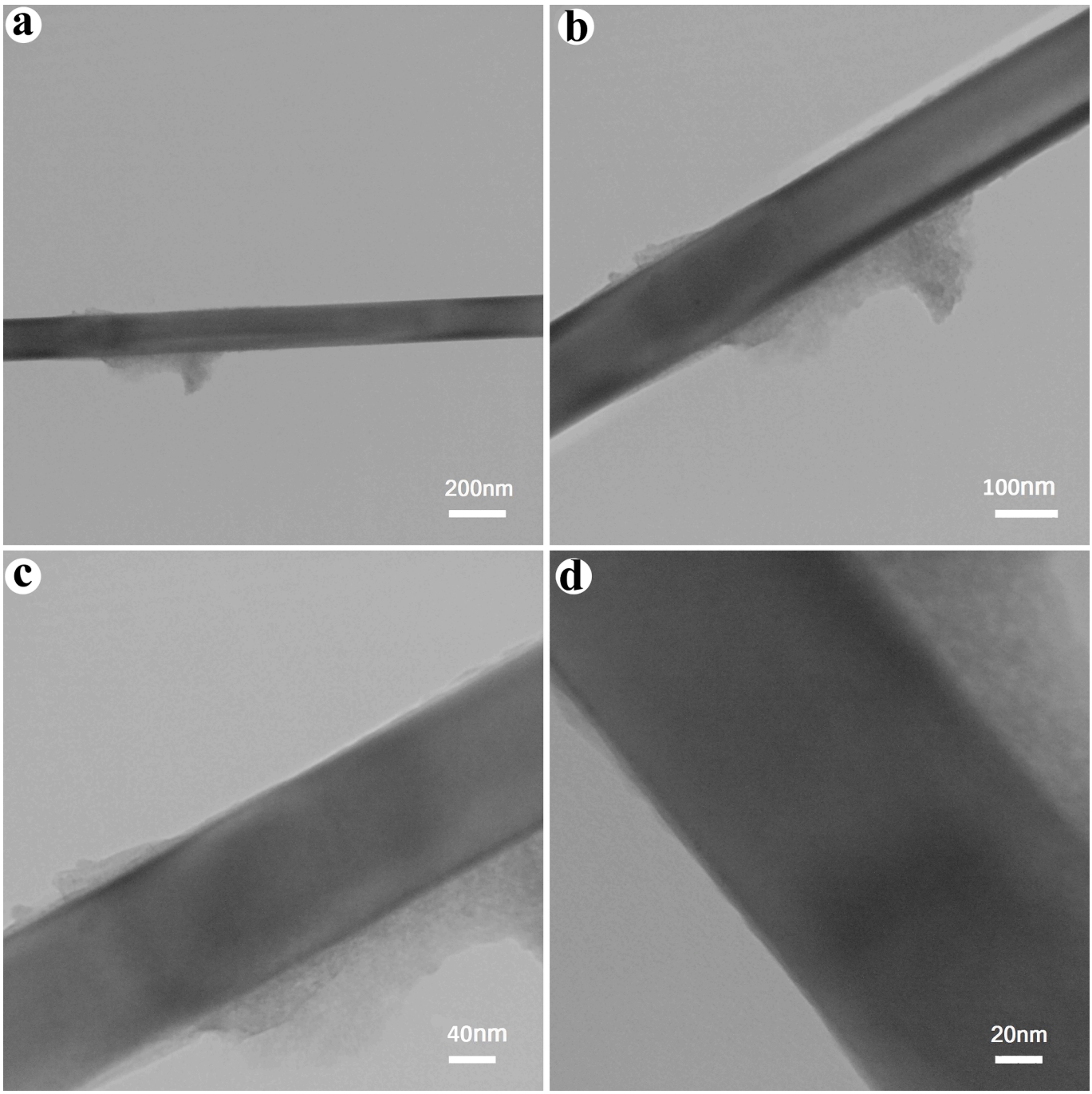

Fig. 6. TEM micrographs of $TmVO_4$ prepared at 30 min, 60 W sonication and 7 h calcination time (sample 9).

adsorption–desorption (ADS-DES) isotherm and BJH curve of $TmVO_4$ can be seen. In accordance with IUPAC categories, the N_2 ADS-DES isotherm belongs to type IV isotherms with H_3 hysteresis loops, which are regarded as being characteristic of ordered mesoporous materials. The pore size distribution for $TmVO_4$ can be seen in Fig. 7b, which shows a broad distribution with a maximum in the vicinity of pores of 29 nm diameter. This sample has a mean pore diameter of 30.73 nm and a total pore volume of 0.1914 cm^3/g, respectively. In addition, the BET analysis indicates a specific surface area of 24.91 m^2/g.

3.6. Optical absorption and magnetic properties

The electronic excitation from the VB to the CB is usually related to the optical absorption, or absorption edge. Therefore, the DRS data can be used to estimate the optical bandgap energy of the subject sample. It is most effective to achieve this objective by using the Kubelka-Maunk (K-M) equation and the Tauc graphs that result from it. In a typical K-M equation, the absolute R-values (in %) are converted into K-values, a measure of the transformed R: [40].

$$K = (1-R)^2/2R \tag{14}$$

Using the Tauc relation, it is possible to calculate the samples' energy band gaps:

$$(\alpha h\upsilon) = \beta(h\upsilon - Eg)^n \tag{15}$$

In Eq. (15), υ and h (6.626×10^{-34} J s) represent the light frequency and Planck constant, respectively. α is the absorption coefficient which depends on the sample thickness (d) and the sample absorbance (A), α=

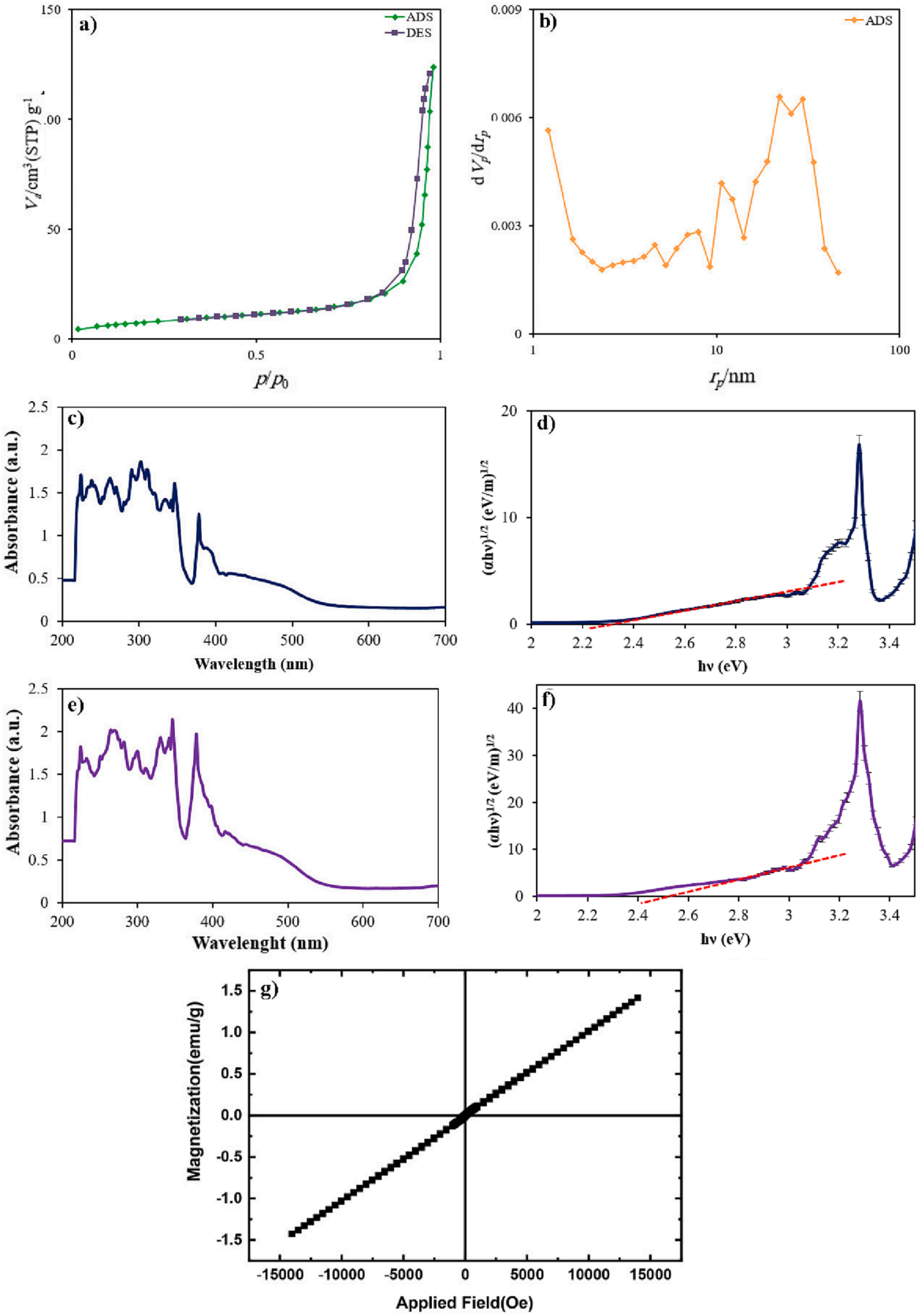

Fig. 7. A) n_2 absorption–desorption, b) BJH plot of $TmVO_4$ prepared at 30 min, 60 W sonication and 7 h calcination time (sample 9), (c, e) UV–Vis DRS spectrum, (d, f) the plot of bandgap energies of samples 4 and 9, and g) VSM plot of $TmVO_4$ prepared at 30 min, 60 W sonication and 7 h calcination time (sample 9).

([2.303 × A]/d). β is the sample absorbance. Depending on the type of electronic transition, the power "n" will vary. In this way, it obtains values of 2 and 1/2 for the permitted indirect and direct electronic transitions, as well as 3 and 3/2 for the forbidden indirect and direct transitions [41]. Based on the diffuse reflectance spectrum (DRS) of samples No. 4 and No. 9, the bandgap energy was calculated. Both samples (Samples No. 4 and 9) have an estimated bandgap of 2.3 eV as the best-prepared samples. A bandgap may be used to determine what kind of light source is required to destroy dyes.

A vibrating sample magnetometer (VSM) is used to characterize the magnetization hysteresis of $TmVO_4$ (sample No. 9) at room temperature (25 °C) (Fig. 7g). During the ideal conditions, the hysteresis loop of the sample exhibits paramagnetic behavior, with a maximum saturation magnetization of 1.417 emu/g.

3.7. Photoactivity of catalyst

3.7.1. Dye effect

The Fig. 8a illustrates the degradation of Eriochrome Black T (EBT) and Methyl Violet (MV) in the presence of $TmVO_4$ nanorods. Using $TmVO_4$ nanorods can induce 50.6% of decoloration of EBT as an anionic dye and 46.6% of decoloration of MV as a cationic dye after 90 min, respectively. As an excellent oxidizing agent, $TmVO_4$ has the capacity to oxidize the anionic dye, Eriochrome Black T, more efficiently and effectively than the cationic dye, methyl violet. Since EBT has a negative charge, it is more susceptible to oxidation by $TmVO_4$ than MV, which has a positive charge. Moreover, the anionic dye has a larger surface area than the cationic dye, which makes it easier for $TmVO_4$ to react with and degrade EBT.

3.7.2. pH effect

In photodegradation efficiency, pH plays a significant role since it influences both the charged species of the pollutant and the accumulated charges on the catalyst surface [42-44]. Photocatalytic efficiencies were investigated in relation to pH of the EBT solutions (Fig. 8b). EBT degradation efficiencies range from 65.6% at pH 10, 7.4% at pH 4, and 38.78% at pH 4. In the photocatalytic process, the pH of the initial solution plays an important role in the uptake of the adsorption capacity. Diprotic dye EBT uptake is most effective at pH = 10, which is the optimal condition for its removal. As a result of monitoring the photocatalytic action between pH 4 and 10, $TmVO_4$ nanorods performed best in alkaline media, while their photocatalytic activity increased at pH 10. We are concerned with two issues in alkaline media: increasing the density of the •OH radical and acquiring a more effective position on the surface of $TmVO_4$. As pH is raised, a greater concentration of •OH functions is produced. In consequence, the generation of •OH radicals in solution increased, and toxic dye was eliminated more effectively. Upon interaction of two hydroxyl radicals, the H_2O_2 and HO_2 radicals were produced. When pH levels are higher, radical reactions occur due to the presence of a large number of •OH radicals. Therefore, a rise in pH is associated with an increase in the efficiency of photocatalytic degradation of toxic dyes. Accordingly, it is possible to infer that pH and decolorization efficacy are directly related.

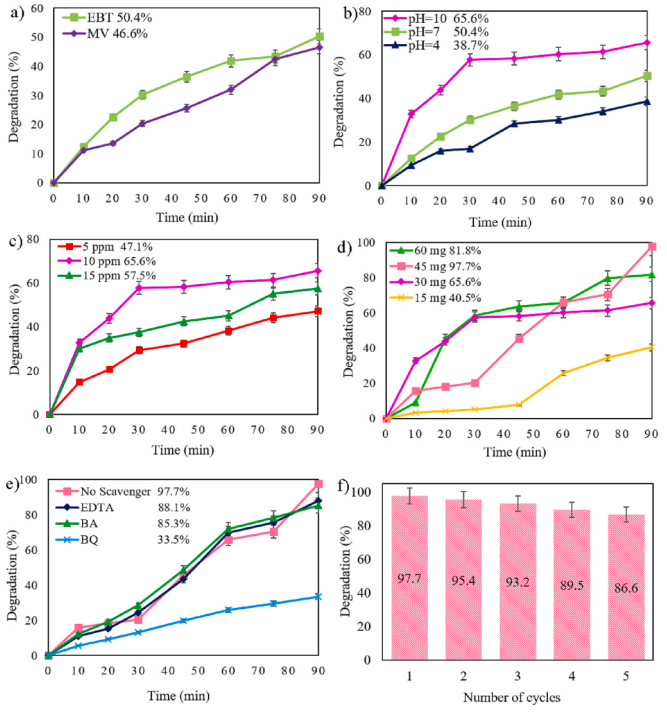

Fig. 8. Photocatalytic degradation of $TmVO_4$ prepared at 30 min, 60 W sonication and 7 h calcination time (sample 9) in the presence of a) Eriochrome black T and methyl violet, b) effect of different pH of the solution, c) different dye concentrations, d) different dosages of catalyst, e) scavenger effect, and f) recyclability under visible radiation. (For interpretation of the references to color in this figure legend, the reader is referred to the web version of this article.)

3.7.3. Dye concentration effect

The photocatalytic activity of $TmVO_4$ nanorods was subsequently assessed over a range of EBT concentrations. According to Fig. According to Fig. 8c, $TmVO_4$ nanorods exhibit approximately 47.1%, 65.6%, and 57.5% activity when EBT is present at 5 ppm, 10 ppm, and 15 ppm under visible light, respectively. A 15 ppm concentration of EBT results in a greater number of EBT molecules saturating binding sites on the surface of $TmVO_4$ nanorods. The removal efficiency percentage decreased as the initial dye concentration increased. Conversely, when the dye concentration is less than a certain level, the number of molecules is too small to be placed on the surface of the catalyst in order to eliminate it.

3.7.4. Catalyst loading effect

An example of a photocatalytic test for verifying the effect of catalyst loading can be found in Fig. 8d. With an increase in catalyst dosage from 15 mg to 30 mg, the photocatalytic efficiency increased from 40.5% to 65.6%. Furthermore, the photocatalytic efficiency was improved from 65.6% to 97.7% by increasing the $TmVO_4$ content from 30 mg to 45 mg. When the $TmVO_4$ loading was increased to 60 mg, the efficiency was decreased to 81.8%%.

Increasing the $TmVO_4$ content led to an increase in $TmVO_4$ surface area and enhanced dye absorption on $TmVO_4$ surfaces. Nevertheless, the increase in catalyst content is only practical to a certain extent (45 mg), and then the nanorod coatings were saturated. The photocatalytic efficiency decreases as $TmVO_4$ nanorods in dye solutions become thicker since they are unable to reach the solution for irradiation. Consequently, loading 45 mg of $TmVO_4$ is the ideal condition for Eriochorme black T degradation..

3.7.5. Comparison study

In Table 2, a comparison of vanadate photocatalysts is provided. It has been demonstrated that nanostructures of $TmVO_4$ are capable of degrading organic dyes with a suitable level of photocatalytic activity.

3.7.6. Scavenger test

A combination of three scavengers, including BA, EDTA, and BQ, were employed to capture, respectively, •OH, h^+, and $\bullet O_2^-$. A comparison of the degradation rates of BA and EDTA to those of no scavenger is shown in Fig. 8e; these degradation rates were approximately 85.3%, 88.1%, and 97.7%, respectively. Therefore, while •OH and h^+ have little effect on the deterioration of $TmVO_4$ nanostructures, $\bullet O_2^-$ has a significant effect.

Table 2
Photocatalytic performance comparison of different vanadate photocatalysts.

Photocatalyst	Method	Targeted Pollutants	Light Source	Reaction Time (min)	Degradation (%)	Ref.
$GdVO_4$/silica fiber	Alcohol -thermal treatment	MB	UV	90	64.5	[45]
$CeVO_4$/silica fiber	Alcohol -thermal treatment	MB	UV	90	48.5	[45]
$NdVO_4$/silica fiber	Alcohol -thermal treatment	MB	UV	90	32.3	[45]
$CeVO_4$	Hydrothermal	RhB	UV	80	65.0	[46]
$HoVO_4$	Sonochemical	MV	UV	90	67.6	[47]
$YbVO_4$	Sonochemical	MB	Visible	120	65.0	[34]
$PrVO_4$	Sonochemical	Erythrosine	UV	90	50. 7	[48]
$SmVO_4$	Sol-gel	carbamazepine	Solar simulator	300	26.6	[49]
$NdVO_4$	Sonochemical	EBT	UV	75	77.4	[36]
$TmVO_4$	Sonochemical	Phenol red	Visible	90	71.7	This work

3.7.7. Recyclability test

$TmVO_4$ nanocatalyst was tested for repeatability in an EBT photodegradation recycling test. After the initial visible exposure, $TmVO_4$ nanorods were typically separated and washed with distilled water. We began the second run of the test by combining the new dye solution with the previously used nanocatalysts. In a similar manner to the initial run, the following four runs of photocatalytic recycling were conducted. As shown in Fig. 8f, the adsorption abilities decreased slightly from 97.7% to 86.6% after five repetitions of the photoactivity test. It is evident from the results that $TmVO_4$ is highly stable. Fig. 9 depicts the XRD pattern of $TmVO_4$ after the recycling test. The diffraction peaks are all attributed to $TmVO_4$ (JCPDS No.082–1975, tetragonal structure). The pattern illustrates the high stability of the $TmVO_4$ structure after five cycles.

3.7.8. Mechanism of photodegradation

On the basis of molecular excitation processes, reasonable mechanisms for dye photodegradation can be proposed. TmVO4 nanorods are excited by light, which causes electrons and holes to form, which can then react with water and oxygen in the environment to create a series of active sites, including •O2 − and •OH radials (Eq. (14) - (16)). As a result of the electron combining with an oxygen molecule, it produces superoxide radicals, and as a result of the hole oxidizing water, it produces hydroxyl radicals [43-46]. As stated in Eqs. (17)– (21), these radicals are necessary for the oxidation of pollutants.

$$TmVO_4 \xrightarrow{h\nu} TmVO_4\left(h^+_{VB} + e^-_{CB}\right) \quad (16)$$

$$h^+_{VB} + H_2O \rightarrow H^+ + \cdot OH \quad (17)$$

$$e^-_{CB} + O_2 \rightarrow \cdot O_2^- \quad (18)$$

$$e^-_{CB} + H^+ + \cdot O_2^- \rightarrow H_2O_2 \quad (19)$$

$$2H^+ + 2\cdot O_2^- \rightarrow H_2O_2 + O_2 \quad (20)$$

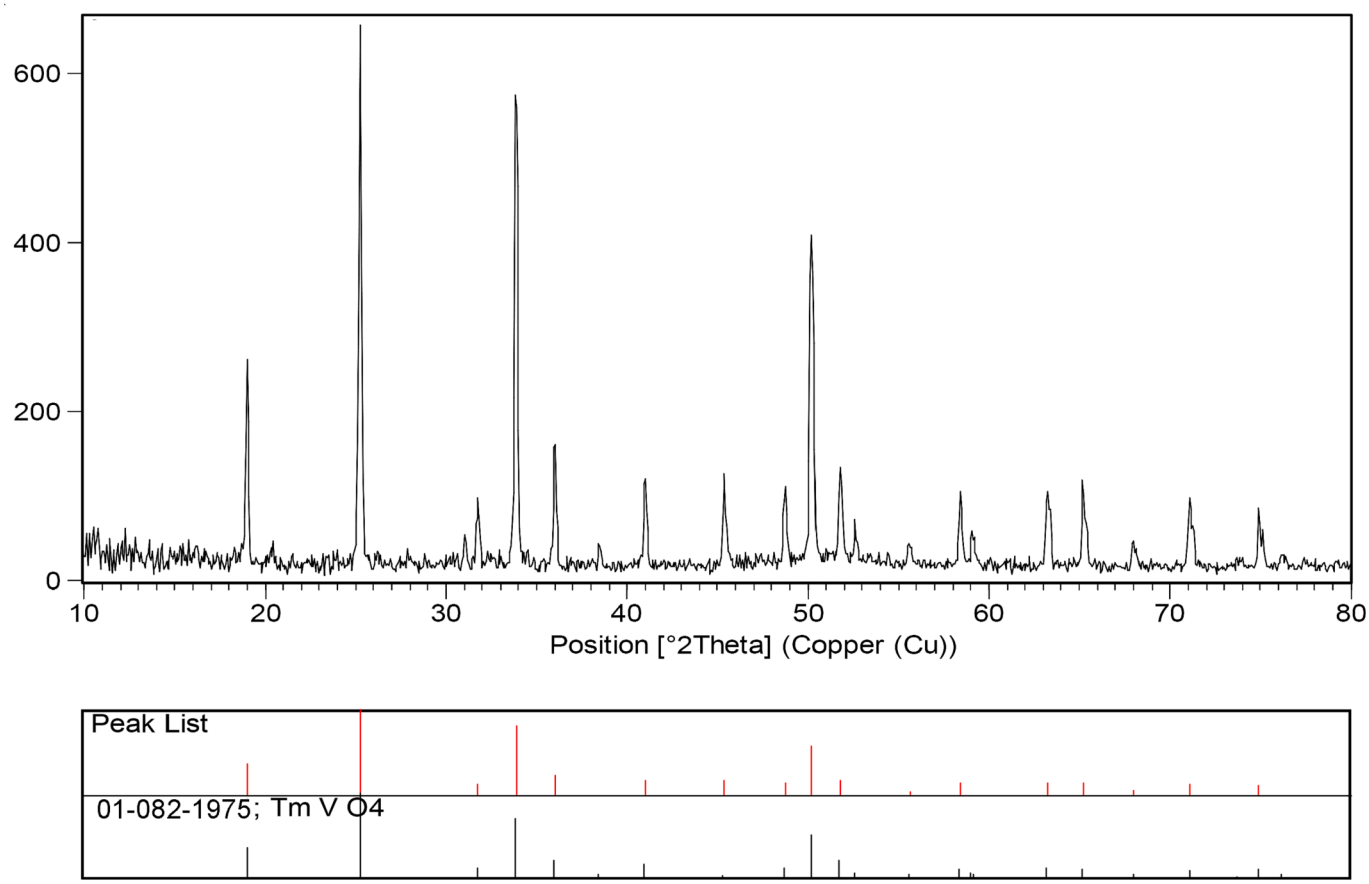

Fig. 9. XRD pattern of TmVO4 after recycling test.

$$e_{CB}^{-} + H_2O_2 \rightarrow \cdot OH + OH^{-} \quad (21)$$

$$EBT + \left(OH\cdot or \cdot O_2^{-}\right) \rightarrow Decolorization\ products + CO_2 + H_2O \quad (22)$$

3.7.9. Kinetic of the process

In order to evaluate the kinetics of typical heterogeneous photocatalytic processes, the Langmuir-Hinshelwood (L-H) model, which is based on the monolayer adsorption of both reactants and products at the solid–liquid interface, has been widely used. A photodegradation process is based on equilibrium adsorption in which the degree of oxidant and reductant adsorption has a significant impact on the contaminant's and its degradation intermediates' photodegradation rates. It should also be noted that the adsorption of these species on the surface of the catalyst is the determining factor in the entire photodegradation procedure [47]. Eq.(3) represents the L-H model, in which r is the reaction rate of oxidation of the reactant/pollutant in mg/L min, k is the specific rate constant of the reaction in mg/L min, K is the equilibrium constant of the reactant in L/mg, and C is the concentration of the reactant/pollutant.

$$r = (dC/dt) = (kKC)/(1 + KC) \quad (23)$$

The Eq.(23), which is commonly used by researchers, can be simplified to its integrated version (Eqs. (24) and 25). Because the catalyst is one of the reactants located in the solid phase and its concentration is constant, this equation is well known for its apparent first-order equation, which is frequently used to describe the kinetics of heterogeneous photodegradation. Here, K' is the apparent first-order rate constant.

$$\ln(C_0/C) - k(C_0 - C) = kKt \quad (24)$$

$$\ln(C_0/C) = kKt = K't \quad (25)$$

In Fig. 10, Hinshelwood plots are shown under a variety of photocatalytic reaction conditions. Therefore, a higher reaction rate constant ($k = 0.0259\ min^{-1}$) was required to obtain superior photocatalytic performance.

4. Conclusions

The purpose of this study was to evaluate promising nano-photocatalysts that were homogeneous and small in size. Thus, H_2Salen was used as a capping agent during the reaction in order to prevent product agglomeration. A number of factors have been altered in order to achieve the desired size and uniformity of the $TmVO_4$ nanorods as they were made. This includes types of Schiff-base ligands, the molar ratio of H_2Salen to metal, sonication power and time, and calcination time. The nanorod morphology of $TmVO_4$ was obtained using a 2:1 ratio of H_2Salen to Tm using a sonication power of 60 W and a calcination time of 30 min at 600 °C. In accordance with BET data, the specific surface area of the sample was 24.91 m^2/g. The bandgap of $TmVO_4$ was calculated by DRS spectroscopy to be 2.3 eV, making it a suitable photocatalyst for visible applications. Various factors, including dye types, pH, TmVO4 loading, and dye concentration, were examined to determine how they affected TmVO4 nanorod photocatalysis. The 45

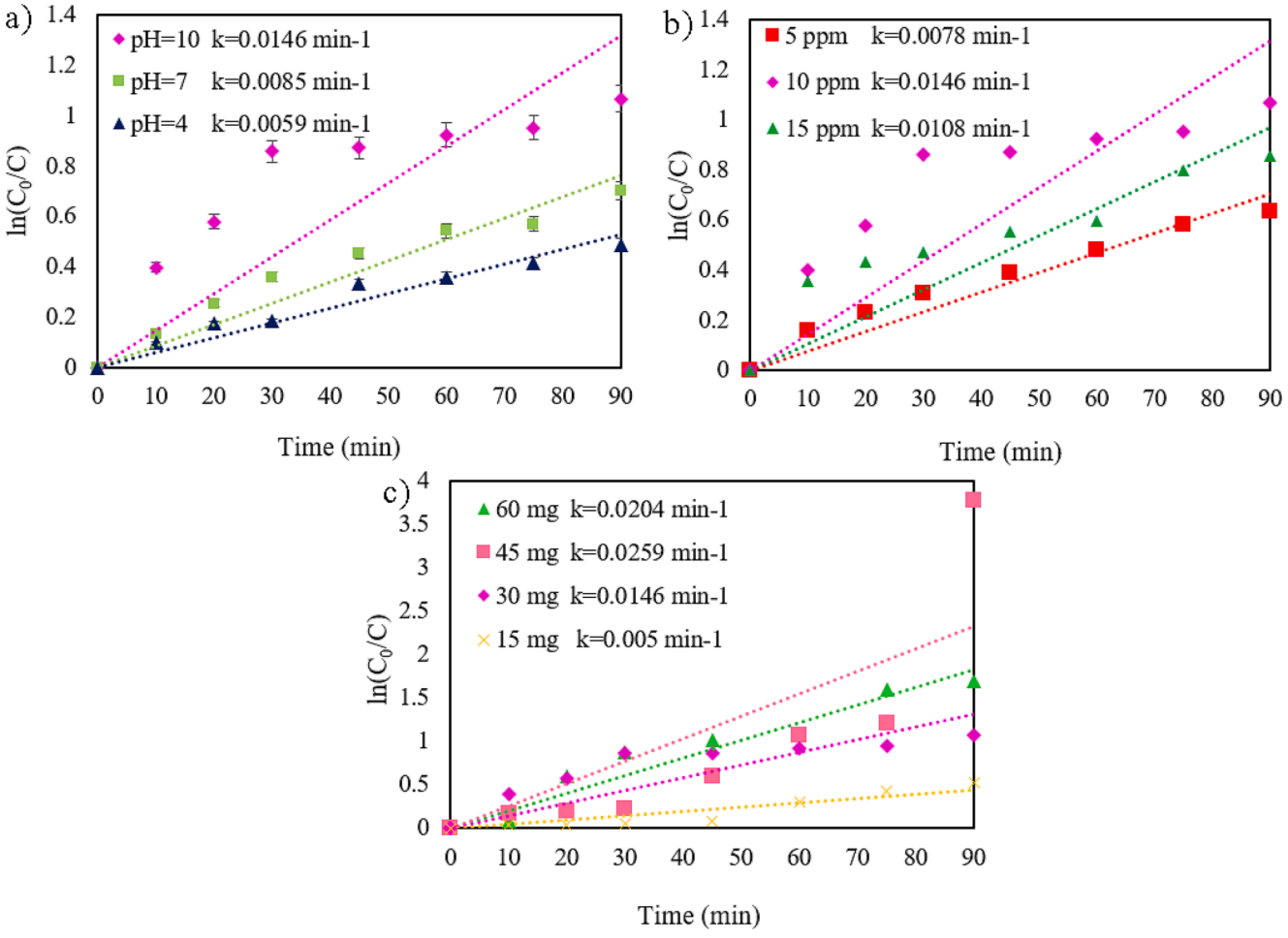

Fig. 10. The resulted Hinshelwood plots of $TmVO_4$ to study the kinetic of the EBT photodegradation process: a) effect of different pH of the solution, b) different dye concentrations, and c) different dosages of catalyst.

mg of $TmVO_4$ demonstrates 97.7% photocatalytic yield over the degradation of 10 ppm EBT at pH = 10 under visible light, suggesting it could be a promising catalyst for improving the catalytic capability for the removal of pollutants. In accordance with our findings, we suggest that $TmVO_4$ nanorods could be used as nano-photocatalysts for dye degradation from effluents. Due to this, we believe $TmVO_4$ nanorods can be utilized as an excellent catalyst in a variety of industries.

Declaration of Competing Interest

The authors declare that they have no known competing financial interests or personal relationships that could have appeared to influence the work reported in this paper.

Acknowledgements

This research was carried out with the support of the University of Kashan (Grant No. 159271/AP4) and the council of Iran National Science Foundation (INSF, 97017837).

References

[1] R. Gusain, K. Gupta, P. Joshi, O.P. Khatri, Adsorptive removal and photocatalytic degradation of organic pollutants using metal oxides and their composites: A comprehensive review, Advances in colloid and interface science 272 (2019), 102009.
[2] S.-X. Gan, C. Jia, Q.-Y. Qi, X. Zhao, A facile and scalable synthetic method for covalent organic nanosheets: ultrasonic polycondensation and photocatalytic degradation of organic pollutants, Chemical Science (2022).
[3] F. Sanakousar, C. Vidyasagar, V. Jiménez-Pérez, K. Prakash, Recent progress on visible-light-driven metal and non-metal doped ZnO nanostructures for photocatalytic degradation of organic pollutants, Materials Science in Semiconductor Processing 140 (2022), 106390.
[4] S.-Y. Hu, Y.-N. Sun, Z.-W. Feng, F.-O. Wang, Y.-K. Lv, Design and construction strategies to improve covalent organic frameworks photocatalyst's performance for degradation of organic pollutants, Chemosphere 286 (2022), 131646.
[5] B. Fu, J. Li, H. Jiang, X. He, Y. Ma, J. Wang, C. Hu, Modulation of electric dipoles inside electrospun BaTiO3@ TiO2 core-shell nanofibers for enhanced piezo-photocatalytic degradation of organic pollutants, Nano Energy 93 (2022), 106841.
[6] K. Karthik, A. Raghu, K.R. Reddy, R. Ravishankar, M. Sangeeta, N.P. Shetti, C. V. Reddy, Green synthesis of Cu-doped ZnO nanoparticles and its application for the photocatalytic degradation of hazardous organic pollutants, Chemosphere 287 (2022), 132081.
[7] H. Hung, C. Halsall, H. Ball, T.F. Bidleman, J. Dachs, A. De Silva, M. Hermanson, R. Kallenborn, D.C. Muir, R. Sühring, Climate change influence on the levels and trends of persistent organic pollutants (POPs) and chemicals of emerging Arctic concern (CEACs) in the Arctic physical environment–a review, Processes & Impacts, Environmental Science, 2022.
[8] C. Simonnet-Laprade, S. Bayen, D. McGoldrick, T. McDaniel, S. Hutinet, P. Marchand, A. Vénisseau, R. Cariou, B. Le Bizec, G. Dervilly, Evidence of complementarity between targeted and non-targeted analysis based on liquid and gas-phase chromatography coupled to mass spectrometry for screening halogenated persistent organic pollutants in environmental matrices, Chemosphere 133615 (2022).
[9] Z.H. Jabbar, S.E. Ebrahim, Recent advances in nano-semiconductors photocatalysis for degrading organic contaminants and microbial disinfection in wastewater: A comprehensive review, Environmental Nanotechnology, Monitoring & Management (2022), 100666.
[10] R. Suresh, S. Rajendran, P.S. Kumar, K. Dutta, D.-V.-N. Vo, Current advances in microbial fuel cell technology toward removal of organic contaminants–A review, Chemosphere 287 (2022), 132186.
[11] A. Waheed, I.W. Kazi, M.S. Manzar, T. Ahmad, M. Mansha, N. Ullah, N.I. Ahmed Blaisi, Ultrahigh and efficient removal of Methyl orange, Eriochrom Black T and acid Blue 92 by triazine based cross-linked polyamine resin: Synthesis, isotherm and kinetic studies, Colloids and Surfaces A: Physicochemical and Engineering Aspects 607 (2020), 125472.
[12] M. Mansha, A. Waheed, T. Ahmad, I.W. Kazi, N. Ullah, Synthesis of a novel polysuccinimide based resin for the ultrahigh removal of anionic azo dyes from aqueous solution, Environmental Research 184 (2020), 109337.
[13] M.S. Manzar, A. Waheed, I.W. Qazi, N.I. Blaisi, N. Ullah, Synthesis of a novel epibromohydrin modified crosslinked polyamine resin for highly efficient removal of methyl orange and eriochrome black T, Journal of the Taiwan Institute of Chemical Engineers 97 (2019) 424–432.
[14] S. Ghattavi, A. Nezamzadeh-Ejhieh, A visible light driven AgBr/g-C3N4 photocatalyst composite in methyl orange photodegradation: Focus on photoluminescence, mole ratio, synthesis method of g-C3N4 and scavengers, Composites Part B: Engineering 183 (2020), 107712.
[15] P. Hemmatpour, A. Nezamzadeh-Ejhieh, A. Ershadi, A brief study on the Eriochrome Black T photodegradation kinetic by CdS/BiVO4 coupled catalyst, Materials Research Bulletin 151 (2022), 111830.
[16] F. Soori, A. Nezamzadeh-Ejhieh, Synergistic effects of copper oxide-zeolite nanoparticles composite on photocatalytic degradation of 2, 6-dimethylphenol aqueous solution, Journal of molecular liquids 255 (2018) 250–256.
[17] S.K. Kansal, S. Sood, A. Umar, S.K. Mehta, Photocatalytic degradation of Eriochrome Black T dye using well-crystalline anatase TiO2 nanoparticles, Journal of Alloys and Compounds 581 (2013) 392–397.
[18] Z. Liu, M.A. Hadi, D.S. Aljuboory, F.A. Ali, M.A. Jawad, A.-A. Ameen, S. K. Hadrawi, T. Mundher, Y. Riadi, R.F. Amer, High efficiency of Ag0 decorated Cu2MoO4 nanoparticles for heterogeneous photocatalytic activation, bactericidal system, and detection of glucose from blood sample, Journal of Photochemistry and Photobiology B: Biology 236 (2022), 112571.
[19] T.H. Abdtawfeeq, Z.A. Farhan, K. Al-Majdi, M.A. Jawad, R.S. Zabibah, Y. Riadi, S. K. Hadrawi, A. AL-Alwany, M.A. Shams,, Ultrasound-Assisted and One-Pot Synthesis of New Fe3O4/Mo-MOF Magnetic Nano Polymer as a Strong Antimicrobial Agent and Efficient Nanocatalyst in the Multicomponent Synthesis of Novel Pyrano [2, 3-d] pyrimidines Derivatives, Journal of Inorganic and Organometallic Polymers and Materials (2022) 1–12.
[20] A.P. de Melo Monteiro, R. Dias Holtz, L. Carneiro Fonseca, C.H. Zanini Martins, M. de Sousa, L.A.V. de Luna, D.L. de Sousa Maia, O.L. Alves, Nano silver vanadate AgVO3: synthesis, new functionalities and applications, The Chemical Record 18 (2018) 973–985.
[21] O. Kumar, M.N. Ashiq, M. Ahmad, S. Anjum, Silver and yttrium-doped bismuth vanadate for photoluminescent activity and boosted visible light-induced photodegradation, Journal of Materials Science: Materials in Electronics 31 (2020) 21082–21096.
[22] M. Casanova, K. Schermanz, J. Llorca, A. Trovarelli, Improved high temperature stability of NH3-SCR catalysts based on rare earth vanadates supported on TiO2WO3SiO2, Catalysis Today 184 (2012) 227–236.
[23] M. Machida, A. Ikematsu, A.S. Nur, H. Yoshida, Catalytic SO3 decomposition activity of SiO2-supported alkaline earth vanadates for solar thermochemical water splitting cycles, ACS Applied Energy Materials 4 (2021) 1696–1703.
[24] S. Osman, S. Zuo, X. Xu, J. Shen, Z. Liu, F. Li, P. Li, X. Wang, J. Liu, Freestanding sodium vanadate/carbon nanotube composite cathodes with excellent structural stability and high rate capability for sodium-ion batteries, ACS Applied Materials & Interfaces 13 (2021) 816–826.
[25] R. Sun, Z. Qin, X. Liu, C. Wang, S. Lu, Y. Zhang, H. Fan, Intercalation Mechanism of the Ammonium Vanadate (NH4V4O10) 3D Decussate Superstructure as the Cathode for High-Performance Aqueous Zinc-Ion Batteries, ACS Sustainable Chemistry & Engineering 9 (2021) 11769–11777.
[26] D. Errandonea, C. Popescu, S.N. Achary, A.K. Tyagi, M. Bettinelli, In situ high-pressure synchrotron X-ray diffraction study of the structural stability in NdVO4 and LaVO4, Materials Research Bulletin 50 (2014) 279–284.
[27] M. Vosoughifar, Synthesis, characterization, and investigation magnetic and photocatalytic property of neodymium vanadate nanoparticles, Journal of Materials Science: Materials in Electronics 27 (2016) 7384–7388.
[28] S. Mahapatra, R. Vinu, T.N.G. Row, G. Madras, Kinetics of photoconversion of cyclohexane and benzene by LnVO4 and LnMo0.15V0.85O4 (Ln=Ce, Pr and Nd), Applied Catalysis A: General 351 (2008) 45–53.
[29] S. Verma, R. Gupta, K.K. Bamzai, Effect of mixing Ce3+ and Nd3+ ions in equimolar ratio on structural, optical and dielectric properties on pure cerium orthovanadate and neodymium orthovanadate, Materials Research Bulletin 81 (2016) 71–84.
[30] H. Deng, S. Yang, S. Xiao, H.-M. Gong, Q.-Q. Wang, Controlled Synthesis and Upconverted Avalanche Luminescence of Cerium(III) and Neodymium(III) Orthovanadate Nanocrystals with High Uniformity of Size and Shape, Journal of the American Chemical Society 130 (2008) 2032–2040.
[31] M.-Y. Ye, Z.-H. Zhao, Z.-F. Hu, L.-Q. Liu, H.-M. Ji, Z.-R. Shen, T.-Y. Ma, 0D/2D Heterojunctions of Vanadate Quantum Dots/Graphitic Carbon Nitride Nanosheets for Enhanced Visible-Light-Driven Photocatalysis, Angewandte Chemie International Edition 56 (2017) 8407–8411.
[32] F.R. Shamskar, F. Meshkani, M. Rezaei, Ultrasound assisted co-precipitation synthesis and catalytic performance of mesoporous nanocrystalline NiO-Al2O3 powders, Ultrasonics Sonochemistry 34 (2017) 436–447.
[33] S. Yuvaraj, R.K. Selvan, V.B. Kumar, I. Perelshtein, A. Gedanken, S. Isakkimuthu, S. Arumugam, Sonochemical synthesis, structural, magnetic and grain size dependent electrical properties of NdVO4 nanoparticles, Ultrasonics sonochemistry 21 (2014) 599–605.
[34] M. Eghbali-Arani, A. Sobhani-Nasab, M. Rahimi-Nasrabadi, F. Ahmadi, S. Pourmasoud, Ultrasound-assisted synthesis of YbVO4 nanostructure and YbVO4/CuWO4 nanocomposites for enhanced photocatalytic degradation of organic dyes under visible light, Ultrasonics Sonochemistry 43 (2018) 120–135.
[35] M. Yousefi, F. Gholamian, D. Ghanbari, M. Salavati-Niasari, Polymeric nanocomposite materials: preparation and characterization of star-shaped PbS nanocrystals and their influence on the thermal stability of acrylonitrile–butadiene, Polyhedron 30 (6) (2011) 1055–1060, https://doi.org/10.1016/j.poly.2011.01.012.
[36] M. Salavati-Niasari, Synthesis and characterization of host (nanodimensional pores of zeolite-Y)–guest [unsaturated 16-membered octaaza–macrocycle manganese (II), cobalt (II), nickel (II), copper, Chemistry letters 34 (10) (2005) 1444–1445, https://doi.org/10.1246/cl.2005.1444.
[37] M. Salavati-Niasari, J. Hasanalian, H. Najafian, Alumina-supported FeCl3, MnCl2, CoCl2, NiCl2, CuCl2, and ZnCl2 as catalysts for the benzylation of benzene by

benzyl chloride, Journal of Molecular Catalysis A: Chemical 209 (1–2) (2004) 209–214, https://doi.org/10.1016/j.molcata.2003.08.027.
[38] M. Salavati-Niasari, A. Amiri, Synthesis and characterization of alumina-supported Mn (II), Co (II), Ni (II) and Cu (II) complexes of bis (salicylaldiminato) hydrazone as catalysts for oxidation of, Applied Catalysis A: General 290 (1–2) (2005) 46–53, https://doi.org/10.1016/j.apcata.2005.05.009.
[39] R. Mahdavi, S.S. Ashraf Talesh, The effect of ultrasonic irradiation on the structure, morphology and photocatalytic performance of ZnO nanoparticles by sol-gel method, Ultrasonics Sonochemistry, 39 (2017) 504-510.
[40] N. Raeisi-Kheirabadi, A. Nezamzadeh-Ejhieh, A Z-scheme g-C3N4/Ag3PO4 nanocomposite: Its photocatalytic activity and capability for water splitting, International Journal of Hydrogen Energy 45 (2020) 33381–33395.
[41] F. Soleimani, A. Nezamzadeh-Ejhieh, Study of the photocatalytic activity of CdS–ZnS nano-composite in the photodegradation of rifampin in aqueous solution, Journal of Materials Research and Technology 9 (2020) 16237–16251.
[42] A.N. Ejhieh, M. Khorsandi, Photodecolorization of Eriochrome Black T using NiS–P zeolite as a heterogeneous catalyst, Journal of Hazardous Materials 176 (2010) 629–637.
[43] K.M. Lee, S.B.A. Hamid, C.W. Lai, Multivariate analysis of photocatalytic-mineralization of Eriochrome Black T dye using ZnO catalyst and UV irradiation, Materials Science in Semiconductor Processing 39 (2015) 40–48.
[44] A. Noruozi, A. Nezamzadeh-Ejhieh, Preparation, characterization, and investigation of the catalytic property of α-Fe2O3-ZnO nanoparticles in the photodegradation and mineralization of methylene blue, Chemical Physics Letters 752 (2020), 137587.
[45] P. Chen, Q. Wu, L. Zhang, W. Yao, Facile immobilization of LnVO4 (Ln= Ce, Nd, Gd) on silica fiber via a combined alcohol-thermal and carbon nanofibers template route, Catalysis Communications 66 (2015) 6–9.
[46] A. Phuruangrat, T. Thongtem, S. Thongtem, Hydrothermal synthesis and characterization of Dy-doped CeVO4 nanorods used for photodegradation of methylene blue and rhodamine B, Journal of Rare Earths 39 (2021) 1211–1216.
[47] M.H. Khorasanizadeh, R. Monsef, O. Amiri, M. Amiri, M. Salavati-Niasari, Sonochemical-assisted route for synthesis of spherical shaped holmium vanadate nanocatalyst for polluted waste water treatment, Ultrasonics sonochemistry 58 (2019), 104686.
[48] R. Monsef, F. Soofivand, H.A. Alshamsi, A. Al-Nayili, M. Ghiyasiyan-Arani, M. Salavati-Niasari, Sonochemical synthesis and characterization of PrVO4/CdO nanocomposite and their application as photocatalysts for removal of organic dyes in water, Journal of Molecular Liquids 336 (2021), 116339.
[49] P.J. Mafa, M.E. Malefane, A.O. Idris, B.B. Mamba, D. Liu, J. Gui, A.T. Kuvarega, Cobalt oxide/copper bismuth oxide/samarium vanadate (Co3O4/CuBi2O4/SmVO4) dual Z-scheme heterostructured photocatalyst with high charge-transfer efficiency: Enhanced carbamazepine degradation under visible light irradiation, Journal of Colloid and Interface Science 603 (2021) 666–684.